

Modelling Axial Nonuniformity in Induction Machines Using a Multi-Slice Magnetic Equivalent Circuit

Zifeng Gong, *Graduate Student Member, IEEE*, Philip Desenfans, Davy Pissoort, *Senior Member, IEEE*, Hans Hallez, *Member, IEEE*, and Dries Vanoost, *Member, IEEE*

Abstract—The presence of axial nonuniformity poses challenges in the modelling of induction machines by disrupting the machine cross-sectional consistency. To tackle these challenges, this article presents a multi-slice magnetic equivalent circuit-based modelling approach. In this model, a machine with axial nonuniformity is partitioned into axially uniform sections along its axial direction, each treated as a slice. The length, angular displacement, and radial translation of each slice are determined using Gaussian discretisation. Magnetic equivalent circuits are constructed for all slices and integrated under an identical current excitation, forming a multi-slice magnetic circuit model. The resultant magnetic circuit equations are combined with temporally discretised electrical circuit equations, establishing a strong electromagnetic coupling. This electromagnetic model is further weakly coupled with a mechanical model to fully characterise machine dynamics, thus completing an electro-magneto-mechanical coupling. The effectiveness of the proposed modelling approach is confirmed through experimental validation.

Index Terms—Axial nonuniformity, induction machines, magnetic equivalent circuits, multi-slice approach.

I. INTRODUCTION

AXIAL nonuniformity in an induction machine (IM) refers to variations in cross-sectional characteristics along the axial direction of the machine. Among the various types of nonuniformity, skewed slots and rotor inclination are particularly prevalent and often coexist, as illustrated in Fig. 1. Skewed slots are widely adopted in IM designs to alleviate permeance harmonics caused by slotting [1], [2], therefore reducing electromagnetic torque ripple, total harmonic distortion of current, mechanical vibration, and acoustic noise produced in IMs. Rotor inclination, also known as axially nonuniform eccentricity, is commonly observed in IMs, whose presence can be mainly attributed to manufacturing imprecision, misalignment, unequal bearing loading, and worn bearings [3], [4]. An inclined rotor leads to an unbalanced magnetic pull (UMP) [5]. This force amplifies motor vibration, accelerating

This work was supported by the China Scholarship Council (No. 202007000007).

Z. Gong, P. Desenfans, D. Pissoort, and D. Vanoost are with Department of Electrical Engineering, M-Group, KU Leuven, Belgium (email: {zifeng.gong; philip.desenfans; davy.pissoort; dries.vanoost}@kuleuven.be). D. Pissoort and D. Vanoost are also with Flanders Make@KU Leuven, Belgium.

H. Hallez is with Department of Computer Science, M-Group, KU Leuven, Belgium (email: hans.hallez@kuleuven.be).

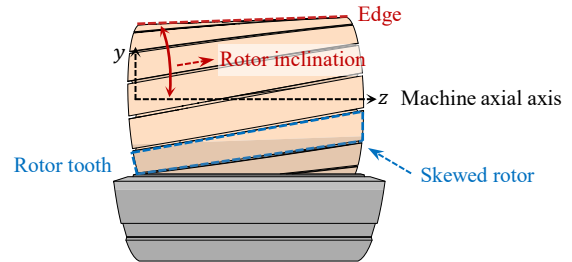


Fig. 1. Side view of an IM with axial nonuniformity.

bearing wear and aggravating eccentricity [6]. Addressing axial nonuniformity in IM modelling benefits improving modelling accuracy and understanding machine intricacies.

The magnetic equivalent circuit (MEC) implemented in this article was initially proposed by Ostović in the 1980s [7]. MEC modelling strikes a balance between finite element modelling [8], [9] and electrical equivalent circuit modelling [4], [10] and offers moderate computational burden and reasonable accuracy. It represents a machine using a geometrically based reluctance network, thereby inherently accounting for spatial dependencies and nonlinear ferromagnetic properties [11]. MECs have been successfully applied to characterise various types of machines, such as squirrel-cage IMs [11], wound rotor synchronous machines [12], single-phase machines [13], permanent magnet machines [14], axial flux machines [15], and switched reluctance machines [16]. Beyond performance analysis, MEC-based approaches have been used to study short circuit faults [17], broken rotor bars [18], and magnet defects [19]. Coupling MECs with sophisticated shaft suspension models allows for investigating the consequences of bearing faults [20], gear box faults [21], and eccentricity-induced UMP [22]. Moreover, hardware-in-the-loop simulations based on MECs using field-programmable gate arrays were explored in [23], [24], showing their potential in computation cost-critical applications such as controller designs and digital twins.

Most MEC-based IM models adhere to the 2D framework introduced in [7], where the most critical and challenging task to account for axial nonuniformity is the parameterisation of equivalent air gap permeance. Prior works, such as [11], [20], [23], [24], have demonstrated the air gap permeance calculation for a machine with skewed slots. For such calculation, all possible tooth overlap scenarios need to be

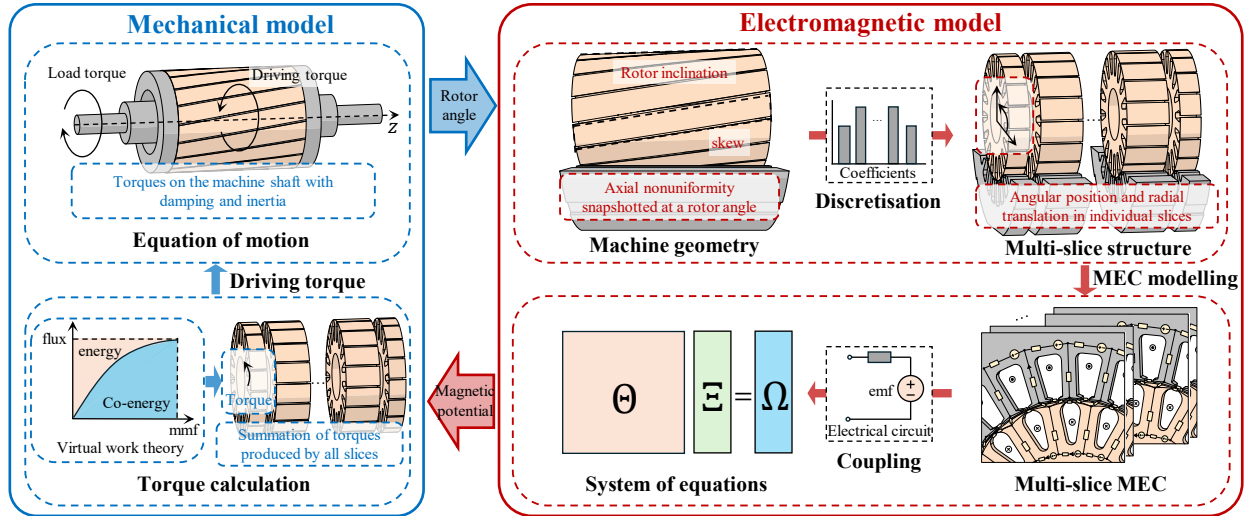


Fig. 2. Overview of the proposed method, which comprises an electromagnetic model and a mechanical model.

enumerated. Moreover, axially nonuniform eccentricity can be modelled by considering an equivalent air gap length, as discussed in [7]. However, enumerating possible tooth overlaps renders this method non-generalisable and accounting for both skewed slots and axially nonuniform eccentricity simultaneously brings significant difficulty in evaluating the permeance expression, which limits the application of this method. Recently, an analytical air gap permeance expression accounting for axially uniform eccentricity was developed in [25], which is built on curve-fitting to a finite element method (FEM). It offers an accurate permeance approximation and preserves analytical expressions of derived torques and UMP. Later, this method was extended in [26] to cover skewed slots. Unfortunately, axially nonuniform eccentricity remains undiscussed.

Besides, an inherent limitation of employing a 2D MEC for modelling axial nonuniformity lies in its inability to represent variations in the flux distribution along the axial direction of a machine, which can be overcome by using 3D MECs [27]–[29]. For instance, a 3D MEC-based IM model was developed in [28], aiming to use MECs as a computer-aided design tool for a 500 W IM. Moreover, a 3D MEC has been reported in [29] to analytically evaluate IM characteristic inductances in the presence of eccentricity. However, despite the remarkable accuracy achieved by 3D MECs, the dramatically increased model complexity significantly increases the computational burden. In addition, the general 3D air gap permeance calculation that accounts for axial nonuniformity can be complex, which may further introduce difficulties in torque and force calculations.

Another promising alternative to address the aforementioned limitations in axial nonuniformity modelling is the multi-slice model structure, which has been widely employed in the FEM-based models [8], [9], [15], [30]. This technique can be considered quasi-3D since it divides a machine into several 2D layers along the shaft, neglecting the axial fluxes. Compared to a 3D FEM-based IM model, a multi-slice FEM-based IM model achieves results with comparable accuracy

while requires significantly less time to solve since the number of variables does not increase substantially. While the multi-slice approach has demonstrated success in FEM-based IM modelling, its implementation in MEC-based IM models to address axial nonuniformity remains scarce. In a broader context, it has been implemented in wound rotor synchronous machines to study the effect of rotor skewing [12], showing the effectiveness of the multi-slice MEC models.

In this article, we address the modelling of an IM with axial nonuniformity using a multi-slice MEC-based approach. As shown in Fig. 2, the proposed method involves an electromagnetic model and a mechanical model. Axial nonuniformity is discretised across all machine slices in the electromagnetic model. These two sub-models are coupled mainly by the magnetic potentials and rotor mechanical angles. The main contributions of this article are summarised as follows.

- 1) The multi-slice structure is incorporated into the MEC-based IM models to capture axial nonuniformity. The governing equations are formulated and the analytical expression of the produced electromagnetic torque is derived.
- 2) The Gaussian discretisation, initially proposed in [30] for determining the length and the angular displacement of each slice for an IM with skew, is extended to handle axially nonuniform eccentricity.
- 3) The electrical and magnetic circuit equations are integrated within the multi-slice structure, resulting in a strong electromagnetic coupling. The global error of the resultant equations due to temporal discretisation is second-order.

Throughout this article, the following notations are used: \mathbb{R} denotes the set of real numbers, \mathbb{Z} denotes the set of integers, A represents a scalar, \mathbf{A} denotes a vector or a matrix, \mathbf{A}^T is the transpose of \mathbf{A} , \mathbf{A}^{-1} is the inverse of \mathbf{A} , $\|\mathbf{A}\|_p$ is the p -norm of \mathbf{A} , $\mathbf{0}$ represents a null matrix.

The remainder of this article is structured as follows. Section II sets forth the model structure. Section III formulates the governing equations. Section IV presents the model integration and solution method. Section V verifies the proposed model. Section VI draws the concluding remarks.

II. MODEL STRUCTURE

This section first outlines the machine discretisation using the multi-slice approach. Subsequently, the magnetic circuit of an arbitrary slice is defined.

A. Multi-Slice Approach

A common practice for organising slices is to use a uniform discretisation, where the total axial length of a machine is equally divided into all slices. However, the findings from [30] have demonstrated that Gaussian discretisation produces a smaller discretisation error than a uniform discretisation for an equal number of slices, where the discretisation coefficients are determined using the Gaussian quadrature approach. This approach is a numerical integration method used to approximate the definite integral of a function $f(\beta)$ in the reference interval $[-1, 1]$ using N points:

$$\int_{-1}^1 f(\beta) d\beta \approx \sum_{k=1}^N \alpha_k f(\beta_k). \quad (1)$$

In (1), α_k are the weights and β_k are the abscissas (see calculations in [31]). The weights sum to 2 and abscissas range from -1 to 1 . Gaussian quadrature is known for its high approximation accuracy and is particularly effective for polynomial functions of degree $2N - 1$ or less since the results are exact. These properties can improve the discretisation accuracy, as, e.g., field wave is an integral of flux density functions over a range of angular positions [30].

Now consider an IM, with a total length of l_z along the z -axis (axial axis), is composed of N slices. The length of the k^{th} slice is given by:

$$l_z^{(k)} = \alpha_k \frac{l_z}{2}, \quad k \in [1, N] \cap \mathbb{Z}. \quad (2)$$

Note that the weights sum to 2 in the Gaussian quadrature approach, i.e., $\sum_{k=1}^N \alpha_k = 2$, which guarantees $\sum_{k=1}^N l_z^{(k)} = l_z$. Moreover, the angular position of each slice can be written as:

$$\theta_r^{(k)} = \theta_r + \beta_k \frac{\gamma}{2}, \quad k \in [1, N] \cap \mathbb{Z}, \quad (3)$$

where θ_r is the rotor position defined at the half-depth of the machine, and γ is the skewing angle.

Furthermore, we extend this method to discretise axially nonuniform eccentricity. Without loss of generality, we consider a rotor with mixed eccentricity being present at both ends. The coordinate (x_f, y_f) of the geometrical centre of the rotor front end surface on the $x - y$ plane (radial plane) can be expressed by:

$$\begin{cases} x_f = g_0 \rho_{mf} \cos \varphi_{mf} \\ y_f = g_0 \rho_{mf} \sin \varphi_{mf} \end{cases}, \quad (4)$$

where g_0 is the normal air gap length of the machine. Additionally, ρ_{mf} and φ_{mf} are the mixed eccentricity degree ($0 \leq \rho_{mf} \leq 1$) and the minimum air gap position ($0 \leq \varphi_{mf} \leq 2\pi$) at the front end, given as the functions of the rotor angular position θ_r :

$$\rho_{mf} = \sqrt{\rho_{sf}^2 + \rho_{df}^2 + 2\rho_{sf}\rho_{df} \cos(\theta_r - \varphi_{sf})}, \quad (5)$$

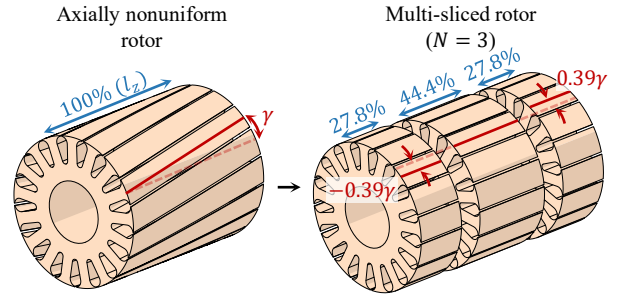


Fig. 3. An illustrative example of rotor axial nonuniformity discretisation with three slices.

and

$$\varphi_{mf} = \varphi_{sf} + \arctan \left(\frac{\rho_{df} \sin(\theta_r - \varphi_{sf})}{\rho_{sf} + \rho_{df} \cos(\theta_r - \varphi_{sf})} \right), \quad (6)$$

where ρ_{sf} and ρ_{df} are the static and dynamic component. φ_{sf} is the position of the static component. Analogously, the coordinate (x_b, y_b) of the centre of the rotor back end surface can be determined based on the static and dynamic eccentricity components, denoted as ρ_{sb} and ρ_{db} , along with the position of the static component φ_{sb} .

Assuming an unbent rotor, the radial displacements along the x - and y -axes of each slice can be expressed as:

$$\begin{cases} r_x^{(k)} = \frac{x_f + x_b}{2} + \beta_k \frac{x_b - x_f}{2} \\ r_y^{(k)} = \frac{y_f + y_b}{2} + \beta_k \frac{y_b - y_f}{2} \end{cases}, \quad k \in [1, N] \cap \mathbb{Z}. \quad (7)$$

An example of the axial nonuniformity discretisation for a skewed IM is depicted in Fig. 3, where the machine is segmented into three slices. By solving Gaussian quadrature coefficients with $N = 3$, one can obtain that the weights α_k , for $k = 1, 2, 3$, are 0.556, 0.889, and 0.556, while the abscissas β_k , for $k = 1, 2, 3$, are -0.775 , 0 , and 0.775 . Furthermore, by substituting these coefficients into (2) and (3), it can be calculated that the lengths of the three slices are roughly $27.8\%l_z$, $44.4\%l_z$, and $27.8\%l_z$, and the angular displacements of the first and third slices relative to the second slice are approximately -0.39γ and 0.39γ , respectively.

Gaussian quadrature is typically effective for integrating smooth functions, meaning the Gaussian discretisation is more suitable for addressing machine axial nonuniformity with continuous geometries, such as the rotor inclination and linear rotor skew shown in Fig. 1. Therefore, Gaussian discretisation is not advocated if a machine features regular discontinuities such as step-skewed rotors, as discontinuities across all slices are difficult to avoid. Moreover, while an unbent rotor is assumed, it is important to note that the developed discretisation approach is ready to accommodate rotor deformation.

B. Magnetic Network Definition

Figure 4 illustrates a sector of the magnetic circuit representing an arbitrary slice of an IM, where the machine magnetic behaviour is approximated by employing geometrically based flux tubes. In this context, \mathcal{R} , \mathcal{P} , u , Φ , and \mathcal{F} denote the reluctance, permeance, magnetic scalar potential,

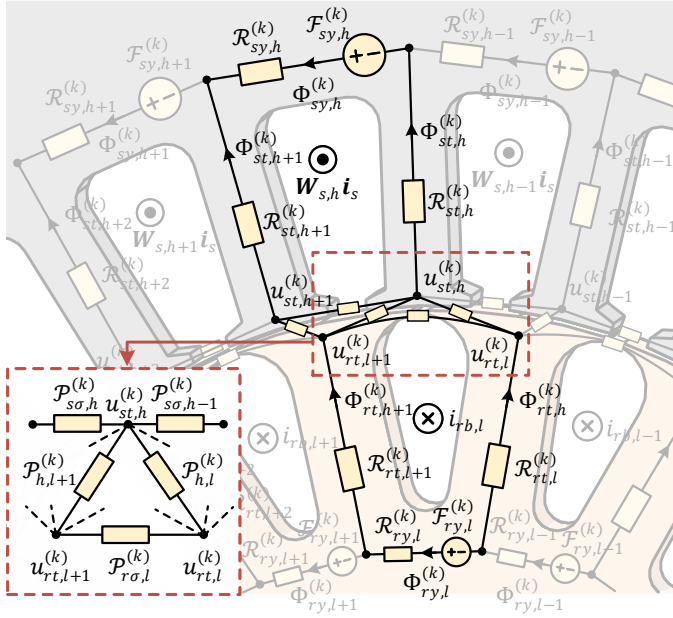


Fig. 4. Magnetic network definition of one machine slice. Nodes are placed in the tooth heads and the yoke segments. Flux paths that link the adjacent nodes are predefined based on the machine working principle. Magnetic circuit excitation is the currents flowing through the slots.

magnetic flux, and magnetomotive force (MMF), respectively. The MMF sources are placed in the stator and rotor yoke segments so their values are directly related to the currents flowing through the corresponding slots, which will be further explained in Section III.

The superscript (k) indicates the association of each symbol involved in the magnetic circuit with the k^{th} slice. The subscripts comprise two parts separated by a comma. In the first part, st , sy , rt , ry , so , and ro serve as the location indicators, representing the stator tooth, stator yoke, rotor tooth, rotor yoke, stator slot, and rotor slot, respectively. The second part includes h and l that are the ring-mapped integer indices for the stator and the rotor. The indices h and l range from 1 to N_s and 1 to N_r , where N_s and N_r are the number of stator and rotor teeth, respectively. One exception in the notation is made for the permeances placed in the air gap, with both two parts in the subscript being ring-mapped indices. For example, $\mathcal{P}_{h,l}^{(k)}$ is the air gap permeance element connecting the stator tooth h and the rotor tooth l .

The majority of the reluctances and the permeances can be calculated based on the IM geometry. Their parametrisation has been detailed in the previous works (e.g., in [7], [11], [25]) and is therefore omitted here. The permeances situated in the air gap are rotor position-dependant and are influenced by the fringing effect and the rotor radial displacement [25]. Their calculation will be elaborated later in Section III. Moreover, though not visualised in the diagram, the stator and rotor leakage fluxes are considered in the flux linkage calculations (20) and (24). The slice angular position $\theta_r^{(k)}$ is defined with respect to the first stator tooth and the first rotor tooth. The counterclockwise direction is defined as the positive direction of rotor rotation.

III. GOVERNING EQUATIONS

This section constructs the circuit equations and coupling equations for the proposed multi-slice MEC.

A. Magnetic Model

According to the MEC presented in Fig. 4, the magnetic potential drops between the two nodes situated in the adjacent stator tooth heads can be expressed as:

$$u_{st,h+1}^{(k)} - u_{st,h}^{(k)} = -\mathcal{R}_{st,h}^{(k)} \Phi_{st,h}^{(k)} + \mathcal{F}_{sy,h}^{(k)} - \mathcal{R}_{sy,h}^{(k)} \Phi_{sy,h}^{(k)} + \mathcal{R}_{st,h+1}^{(k)} \Phi_{st,h+1}^{(k)}, \quad h \in [1, N_s] \cap \mathbb{Z}, \quad (8)$$

where the MMF $\mathcal{F}_{sy,h}^{(k)}$ depends on the current and the number of conductors in the slot:

$$\mathcal{F}_{sy,h}^{(k)} = W_{s,h} i_s. \quad (9)$$

In (9), $W_{s,h} \in \mathbb{R}^{1 \times 3}$ contains the number of turns of all three phases in the h^{th} slot and $i_s \in \mathbb{R}^{3 \times 1}$ is the stator current vector. In addition, applying Gauss's law to stator yoke nodes leads to:

$$-\Phi_{st,h+1}^{(k)} + \Phi_{sy,h+1}^{(k)} - \Phi_{sy,h}^{(k)} = 0, \quad h \in [1, N_s - 1] \cap \mathbb{Z}. \quad (10)$$

Similar to (8), the derived potential drops in the rotor circuit can be written as:

$$u_{rt,l+1}^{(k)} - u_{rt,l}^{(k)} = \mathcal{R}_{rt,l}^{(k)} \Phi_{rt,l}^{(k)} + \mathcal{F}_{ry,l}^{(k)} - \mathcal{R}_{ry,l}^{(k)} \Phi_{ry,l}^{(k)} - \mathcal{R}_{rt,l+1}^{(k)} \Phi_{rt,l+1}^{(k)}, \quad l \in [1, N_r] \cap \mathbb{Z}. \quad (11)$$

In (11), the MMF $\mathcal{F}_{ry,l}^{(k)}$ is numerically equal to the current in the l^{th} rotor bar, which is denoted as $i_{rb,l}$:

$$\mathcal{F}_{ry,l}^{(k)} = i_{rb,l}. \quad (12)$$

The rotor tooth and yoke fluxes are related by:

$$\Phi_{rt,l+1}^{(k)} + \Phi_{ry,l+1}^{(k)} - \Phi_{ry,l}^{(k)} = 0, \quad l \in [1, N_r] \cap \mathbb{Z}. \quad (13)$$

Furthermore, Gauss's law applied to one stator tooth node and one rotor tooth node yields:

$$\Phi_{st,h}^{(k)} + \mathcal{P}_{so,h}^{(k)} (u_{st,h}^{(k)} - u_{st,h+1}^{(k)}) - \mathcal{P}_{so,h-1}^{(k)} (u_{st,h-1}^{(k)} - u_{st,h}^{(k)}) - \sum_{m=1}^{N_r} \mathcal{P}_{h,m}^{(k)} (u_{rt,m}^{(k)} - u_{st,h}^{(k)}) = 0, \quad h \in [1, N_s] \cap \mathbb{Z}, \quad (14)$$

and

$$-\Phi_{rt,l}^{(k)} + \mathcal{P}_{ro,l}^{(k)} (u_{rt,l}^{(k)} - u_{rt,l+1}^{(k)}) - \mathcal{P}_{ro,l-1}^{(k)} (u_{rt,l-1}^{(k)} - u_{rt,l}^{(k)}) + \sum_{m=1}^{N_s} \mathcal{P}_{m,l}^{(k)} (u_{rt,l}^{(k)} - u_{st,m}^{(k)}) = 0, \quad l \in [1, N_r] \cap \mathbb{Z}. \quad (15)$$

The air gap permeances in (14) and (15) are calculated using the analytical model developed in [25], which is built on curve-fitting to a FEM. Specifically, the permeance $\mathcal{P}_{h,l}^{(k)}$ connecting the stator tooth h and the rotor tooth l is given as:

$$\mathcal{P}_{h,l}^{(k)} = \frac{\mathcal{P}_0^{(k)} g_0}{g_h^{(k)}} e^{-\left(\frac{\gamma_{h,l}^{(k)}}{\theta_{st}^{(k)}}\right)^2 - \left(\frac{\gamma_{h,l}^{(k)}}{\theta_{rt}^{(k)}}\right)^2}, \quad (16)$$

where $\gamma_{h,l}^{(k)}$ is the angular distance between the two teeth, $\mathcal{P}_0^{(k)}$ the mean air gap permeance neglecting fringing for $\gamma_{h,l}^{(k)} = 0$, $g_h^{(k)}$ the effective air gap length, θ_{th}^{st} the angle spanned by the stator tooth head, θ_{th}^{rt} the angle spanned by the rotor tooth head. Since fluxes tend to flow through the path with the least reluctance, the effective air gap length $g_h^{(k)}$ can be calculated from the geometry:

$$g_h^{(k)} = \sqrt{\left(r_{in}^{st} \cos \alpha_h^{(k)} - r_x^{(k)}\right)^2 + \left(r_{in}^{st} \sin \alpha_h^{(k)} - r_y^{(k)}\right)^2 - r_{out}^{rt}}, \quad h \in [1, N_s] \cap \mathbb{Z}, \quad (17)$$

where $\alpha_h^{(k)}$ is the angular position of the h^{th} stator tooth, r_{in}^{st} the stator inner radius, r_{out}^{rt} the rotor outer radius. In addition, $r_x^{(k)}$ and $r_y^{(k)}$ denote the horizontal and vertical rotor translations, as given in (7).

In addition, to guarantee a unique solution, the magnetic scalar potential of the first stator tooth node is set to zero as a reference:

$$u_{st,1}^{(k)} = 0. \quad (18)$$

B. Electrical Model

The circuit equations of stator phase windings are given by:

$$v_m = R_m i_m + \frac{d\lambda_m}{dt}, \quad m \in [1, 3] \cap \mathbb{Z}, \quad (19)$$

where v_m , i_m , and R_m denote the stator phase voltage, phase current, and winding resistance, respectively. Moreover, λ_m denotes the stator phase flux linkage, as given by:

$$\lambda_m = \sum_{k=1}^N \sum_{h=1}^{N_s} S_{m,h} \Phi_{st,h}^{(k)} + L_{\sigma m} i_m, \quad (20)$$

where $L_{\sigma m}$ is the stator leakage inductance and $S_{m,h}$ is the m^{th} element in the h^{th} column of the flux transformation matrix. The flux transformation matrix is calculated from the machine winding arrangement, as presented in [11].

Equation (19) is suitable for stator windings connected in a "delta" or in a "star" with a connected neutral point, since in both cases phase voltages are typically known. For windings connected in a "star" with an isolated neutral point, line voltages v_m ($m \in [1, 3] \cap \mathbb{Z}$) should be used as the input. They are related to the phase voltages by:

$$\begin{bmatrix} 0 & 0 & -1 \\ -1 & 0 & -1 \end{bmatrix} \begin{bmatrix} v_1 \\ v_2 \\ v_3 \end{bmatrix} = \begin{bmatrix} 1 & 0 & -1 \\ 0 & 1 & -1 \end{bmatrix} \begin{bmatrix} v_1 \\ v_2 \\ v_3 \end{bmatrix}. \quad (21)$$

Moreover, in this scenario, an additional constraint on phase currents is added such that the currents comply with the Kirchhoff's circuit law:

$$\sum_{m=1}^3 i_m = 0. \quad (22)$$

Replacing phase voltages with line voltages in (19) using (21) and combining the resultant equations with (22) lead to the stator electrical circuit equations for "star" connected windings with an isolated neutral point.

Furthermore, the circuit equation for each rotor loop can be written as:

$$\frac{d\lambda_{rt,l}}{dt} = -R_{rb,l-1} i_{rb,l-1} + 2R_{rr,l} i_{rr,l} + R_{rb,l} i_{rb,l}, \quad l \in [1, N_r - 1] \cap \mathbb{Z}, \quad (23)$$

where $i_{rr,l}$ is the current in the l^{th} rotor ring segment, $R_{rb,l}$ the resistance of the l^{th} rotor bar, $R_{rr,l}$ the resistance of the end ring segment connecting the $(l-1)^{\text{th}}$ bar and the l^{th} bar. Moreover, the flux linkage $\lambda_{rt,l}$ in (23) is given by:

$$\lambda_{rt,l} = \sum_{k=1}^N \Phi_{rt,l}^{(k)} + \mathcal{P}_{rb,l} i_{rb,l} + 2\mathcal{P}_{rr,l} i_{rr,l} - \mathcal{P}_{rb,l-1} i_{rb,l-1}, \quad (24)$$

where $\mathcal{P}_{rb,l}$ and $\mathcal{P}_{rr,l}$ are the permeances of the flux paths in the rotor bar and the ring segment. The Kirchhoff's current law applied to the nodes placed in the ring segment yields:

$$i_{rb,l} = i_{rr,l} - i_{rb,l+1}, \quad l \in [1, N_r - 1] \cap \mathbb{Z}. \quad (25)$$

Assuming undamaged rotor rings, i.e., all ring segment resistances $R_{rr,l}$ are equal, the ring currents $i_{rr,l}$ can be eliminated by manipulating (23), (24), and (25), giving rise to:

$$\frac{d(\lambda_{rt,l+1} - \lambda_{rt,l})}{dt} = -2(R_{rb,l} + R_{rr,l}) i_{rb,l} + R_{rb,l+1} i_{rb,l+1} + R_{rb,l-1} i_{rb,l-1}, \quad (26)$$

and

$$\lambda_{rt,l+1} - \lambda_{rt,l} = \sum_{k=1}^N (\Phi_{rt,l+1}^{(k)} - \Phi_{rt,l}^{(k)}) - 2(\mathcal{P}_{rb,l} + \mathcal{P}_{rr,l}) i_{rb,l} + \mathcal{P}_{rb,l+1} i_{rb,l+1} + \mathcal{P}_{rb,l-1} i_{rb,l-1}. \quad (27)$$

Since rotor bars are shortened by end rings, the summation of rotor bar currents is equal to zero:

$$\sum_{l=1}^{N_r} i_{rb,l} = 0. \quad (28)$$

C. Mechanical Model

The equation of shaft motion can be formulated as:

$$J \frac{d^2 \theta_r}{dt^2} + D \frac{d\theta_r}{dt} = T_e - T_l, \quad (29)$$

where J is the rotor inertia, D the rotational damping, T_e the total produced torque, T_l the load torque.

The virtual work theory determines the produced torque by taking the partial derivative of the magnetic co-energy with respect to the rotor angle. For each machine slice, the magnetic co-energy stored in the air gap, denoted as $W_{co}^{(k)}$, is given by:

$$W_{co}^{(k)} = \frac{1}{2} \sum_{h=1}^{N_s} \sum_{l=1}^{N_r} \left(u_{rt,l}^{(k)} - u_{st,h}^{(k)}\right)^2 \mathcal{P}_{h,l}^{(k)}. \quad (30)$$

Accordingly, the torque produced by the k^{th} machine slice is given by:

$$T_e^{(k)} = \frac{\partial W_{co}^{(k)}}{\partial \theta_r} = \frac{1}{2} \sum_{h=1}^{N_s} \sum_{l=1}^{N_r} \left(u_{rt,l}^{(k)} - u_{st,h}^{(k)}\right)^2 \frac{\partial \mathcal{P}_{h,l}^{(k)}}{\partial \theta_r}. \quad (31)$$

Note that:

$$\frac{\partial \mathcal{P}_{h,l}^{(k)}}{\partial \theta_r} = \frac{\partial \mathcal{P}_{h,l}^{(k)}}{\partial \theta_r^{(k)}} \frac{\partial \theta_r^{(k)}}{\partial \theta_r} = \frac{\partial \mathcal{P}_{h,l}^{(k)}}{\partial \theta_r^{(k)}}. \quad (32)$$

This partial derivative is analytically solvable, as given by:

$$\frac{\partial \mathcal{P}_{h,l}^{(k)}}{\partial \theta_r^{(k)}} = \frac{-2\mathcal{P}_0^{(k)} g_0 \gamma_{h,l}^{(k)} \theta_{th}^{st2} + \theta_{th}^{rt2}}{g_h^{(k)} (\theta_{th}^{st} \theta_{th}^{rt})^2} e^{-\left(\frac{\gamma_{h,l}^{(k)}}{\theta_{th}^{st}}\right)^2} - \left(\frac{\gamma_{h,l}^{(k)}}{\theta_{th}^{rt}}\right)^2. \quad (33)$$

Therefore, the total produced electromagnetic torque T_e is the summation of the torques produced by each individual slice:

$$T_e = \sum_{k=1}^N T_e^{(k)} = \frac{1}{2} \sum_{k=1}^N \sum_{h=1}^{N_s} \sum_{l=1}^{N_r} (u_{rt,l}^{(k)} - u_{st,h}^{(k)})^2 \frac{\partial \mathcal{P}_{h,l}^{(k)}}{\partial \theta_r^{(k)}}. \quad (34)$$

Similarly, the horizontal UMP and vertical UMP experienced by the rotor can be evaluated by taking the derivative of magnetic co-energy with respect to rotor horizontal and vertical translations, respectively.

IV. MODEL INTEGRATION AND SOLUTION

This section first sets forth the temporal discretisation of the differential equations and the assembly of the electromagnetic model. Subsequently, the solution method to the proposed model and the simulation flow are presented.

A. Temporal Discretisation

Both the stator and rotor electrical circuit equations are temporally discretised using the second-order implicit Runge-Kutta method. For a given step-size τ , the stator circuit differential equations (19) can be discretised as:

$$\lambda_m[n+1] + \frac{\tau}{2} R_s i_m[n+1] = \frac{\tau}{2} \lambda_m[n] (v_m[n+1] + v_m[n] - R_s i_m[n]), \quad (35)$$

where n represents the discrete time index. The temporal discretisation of the rotor circuit equations (26) is similar to (35) and omitted here. Note that all terms on the right hand side of these discretised differential circuit equations are known when solving for the unknown quantities at the step $n+1$. Hence, it is feasible to couple these equations with the magnetic circuit algebraic equations, allowing for implementing a time-stepping.

The equation of motion (29) is converted to two first-order differential equations and discretised as:

$$\begin{cases} \omega_r[n+1] = (1 - \frac{\tau D}{J}) \omega_r[n] + \frac{1}{J} (T_e[n] - T_l[n]), \\ \theta_r[n+1] = \theta_r[n] + \tau \omega_r[n] \end{cases}, \quad (36)$$

where ω_r is the mechanical rotor speed.

B. Electromagnetic Model Assembly

For a clearer representation, we introduce the vectors denoted as $\mathbf{u}_{st}^{(k)}$, $\Phi_{st}^{(k)}$, $\Phi_{sy}^{(k)}$, $\mathbf{u}_{rt}^{(k)}$, $\Phi_{rt}^{(k)}$, $\Phi_{ry}^{(k)}$, \mathbf{i}_s , and \mathbf{i}_{rb} . These vectors succinctly organise the corresponding quantities. For example, $\mathbf{u}_{st}^{(k)} \in \mathbb{R}^{N_s \times 1}$ is given by:

$$\mathbf{u}_{st}^{(k)} = [u_{st,1}^{(k)}, u_{st,2}^{(k)}, \dots, u_{st,N_s}^{(k)}]^T. \quad (37)$$

Furthermore, we define composite vectors that are denoted by $\mathbf{x}^{(k)} \in \mathbb{R}^{(3N_s+3N_r) \times 1}$ and $\mathbf{y} \in \mathbb{R}^{(3+N_r) \times 1}$:

$$\mathbf{x}^{(k)} = [\mathbf{u}_{st}^{(k)T}, \Phi_{st}^{(k)T}, \Phi_{sy}^{(k)T}, \mathbf{u}_{rt}^{(k)T}, \Phi_{rt}^{(k)T}, \Phi_{ry}^{(k)T}]^T, \quad (38)$$

and

$$\mathbf{y} = [\mathbf{i}_s^T, \mathbf{i}_{rb}^T]^T. \quad (39)$$

First, the $3+N_r-1$ discrete-time circuit equations, obtained from (19) and (26), can be organised as:

$$\sum_{k=1}^N \mathbf{A}_x^{(k)} \mathbf{x}^{(k)} + \mathbf{A}_y \mathbf{y} = \mathbf{z}, \quad (40)$$

where $\mathbf{z} \in \mathbb{R}^{(3+N_r-1) \times 1}$ is the known vector that is related to the voltages and the flux linkages. Second, the $3N_s+3N_r$ MEC equations, namely (8), (10), (11), (13), (14), (15), and (18), can be organised as:

$$\mathbf{B}_x^{(k)} \mathbf{x}^{(k)} + \mathbf{B}_y^{(k)} \mathbf{y} = \mathbf{0}, \quad k \in [1, N] \cap \mathbb{Z}. \quad (41)$$

Last, the rotor bar current equation (25) can be expressed as:

$$\mathbf{C}_y \mathbf{y} = 0. \quad (42)$$

In (40), (41), and (42), $\mathbf{A}_x^{(k)}$, \mathbf{A}_y , $\mathbf{B}_x^{(k)}$, $\mathbf{B}_y^{(k)}$, and \mathbf{C}_y are the coefficient matrices with proper dimensions.

Combining (40), (41), and (42) leads to the system of equations $\Theta \Xi = \Omega$ which characterises the electromagnetic behaviour of a voltage-fed IM with N axial slices:

$$\underbrace{\begin{bmatrix} \mathbf{A}_x^{(1)} & \mathbf{A}_x^{(2)} & \dots & \mathbf{A}_x^{(N)} & \mathbf{A}_y \\ \mathbf{B}_x^{(1)} & \mathbf{0} & \dots & \mathbf{0} & \mathbf{B}_y^{(1)} \\ \mathbf{0} & \mathbf{B}_x^{(2)} & \dots & \mathbf{0} & \mathbf{B}_y^{(2)} \\ \vdots & \vdots & \ddots & \vdots & \vdots \\ \mathbf{0} & \mathbf{0} & \dots & \mathbf{B}_x^{(N)} & \mathbf{B}_y^{(N)} \\ \mathbf{0} & \mathbf{0} & \dots & \mathbf{0} & \mathbf{C}_y \end{bmatrix}}_{\Theta} \underbrace{\begin{bmatrix} \mathbf{x}^{(1)} \\ \mathbf{x}^{(2)} \\ \vdots \\ \mathbf{x}^{(N)} \\ \mathbf{y} \end{bmatrix}}_{\Xi} = \underbrace{\begin{bmatrix} \mathbf{z} \\ \mathbf{0} \\ \mathbf{0} \\ \vdots \\ \mathbf{0} \\ \mathbf{0} \end{bmatrix}}_{\Omega}, \quad (43)$$

where Θ is the coefficient matrix, Ξ the solution vector, Ω the constant vector. This system of equations comprises $3+N_r+N(3N_s+3N_r)$ equations and unknowns in total.

C. Solution Method

Although appearing similar to a linear matrix equation, the system of equations (43) necessitates an iterative solving approach due to the nonlinearity arising from saturation effects. Specifically, the reluctance of the lumped ferromagnetic material elements is magnetic flux-dependent, meaning that the coefficient matrix Θ has dependency on the solution vector Ξ .

Here, we use the Newton-Raphson method to solve the system of equations (43). First, we define \mathbf{F} as:

$$\mathbf{F} = \Theta \Xi - \Omega. \quad (44)$$

Accordingly, the aim shifts to finding the root of \mathbf{F} in (44) at every time step through a number of iterations. Second, the solution vector can be updated as:

$$\Xi_{p+1} = \Xi_p + \delta (\Xi_p - \mathbf{J}_p^{-1} \mathbf{F}_p), \quad (45)$$

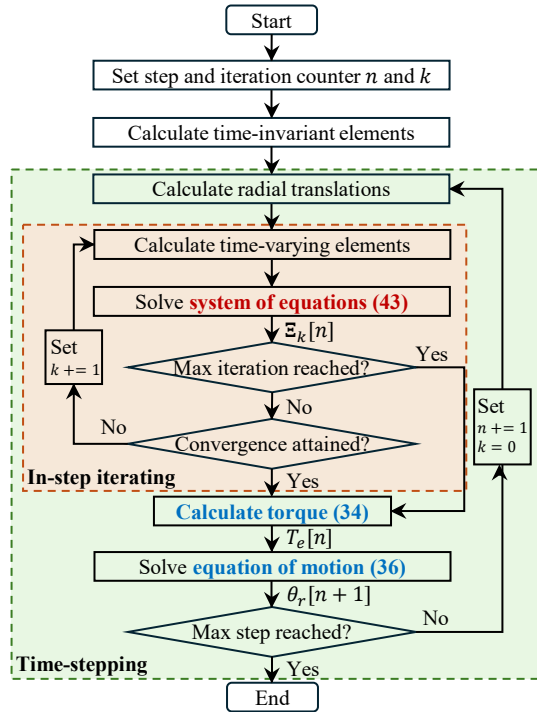


Fig. 5. Simulation flowchart of the proposed modelling approach.

where p denotes the iteration index. The Jacobian matrix \mathbf{J} is given by:

$$\mathbf{J} = \frac{\partial \mathbf{F}}{\partial \boldsymbol{\Xi}} = \frac{\partial \boldsymbol{\Theta}}{\partial \boldsymbol{\Xi}} \boldsymbol{\Xi} + \boldsymbol{\Theta}. \quad (46)$$

Additionally, δ is the damping factor aimed to avoid numerical instability, designed as:

$$\delta = \gamma_1 e^{\gamma_2 p} + \gamma_3, \quad (47)$$

where γ_1 , γ_2 , and γ_3 are the hyperparameters that control the speed of convergence. Last, the convergence is considered attained if the ℓ^2 norm of \mathbf{F} falls below the pre-defined threshold ϵ :

$$\|\mathbf{F}\|_2 < \epsilon. \quad (48)$$

Note that the only nonlinearity arises from the dependency of the reluctance of the lumped ferromagnetic elements on the flux, implying that most entries in $\frac{\partial \boldsymbol{\Theta}}{\partial \boldsymbol{\Xi}}$ are equal to zero. The non-zero terms can be evaluated based on:

$$\frac{d\mathcal{R}}{d\Phi} = \frac{d\mathcal{R}}{d\mu} \frac{d\mu}{d\Phi} = \frac{d\frac{L}{\mu A}}{d\mu} \frac{d\mu}{dBA} = -\frac{L}{A^2} \frac{1}{\mu^2} \frac{d\mu}{dB}, \quad (49)$$

where \mathcal{R} is the reluctance, Φ the flux, B the flux density, μ the permeability, L the length of the flux tube, A the cross-section of the flux tube. Additionally, both μ and $\frac{d\mu}{dB}$ can be evaluated according to the ferromagnetic material B-H curve for a given flux Φ .

D. Simulation Flow

Figure 5 illustrates the simulation flow of the proposed method. Specifically, at each time step, the system of electromagnetic equations (43) is solved iteratively as mentioned

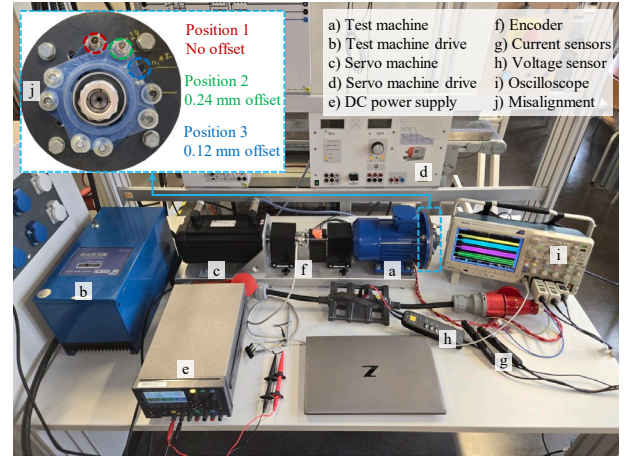


Fig. 6. Experimental setup.

above. Its solution is used to evaluate the produced electromagnetic torque using (34). This torque, in turn, determines the rotor angle for the next time step by solving the equation of motion (36). The updated rotor angle is essential for evaluating the radial translations and air gap permeances involved in the electromagnetic model at the subsequent step. Moreover, a maximum number of iterations is set to prevent excessively long solving procedure. Therefore, a time-stepping iteration is established.

V. RESULTS AND DISCUSSION

This section discusses the selection of the number of slices in the proposed model and verifies the model by comparing its results with the measured data in two scenarios: the fault-free case (skew only) and the eccentric case (both skew and axially nonuniform eccentricity).

The experimental setup is shown in Fig. 6. The machine under investigation is a 400 V, 50 Hz, 1.1 kW, one-pole-pair, double-end squirrel cage IM, with its rotor skewed by one slot. The machine parameters are listed in Table I. The test machine is supplied by an inverter and loaded by a servo machine. Notably, its safety bearing at the non-load end is removed. The injected axially nonuniform eccentricity fault can be controlled by changing the installation positions of the external bearing. The 0.12 mm and 0.24 mm offsets correspond to roughly 25% and 50% static eccentricity. The stator phase winding currents and line voltage were measured using the current probes (Tektronix TCP0030A) and voltage probe (Tektronix THDP0200), respectively. The rotor mechanical speed was measured using the encoder (Kübler 8.5020.8842.1024) powered by the DC supply (Keysight E36313A). The measured quantities were displayed and recorded using the oscilloscope (Tektronix DPO3054).

In this section, unless otherwise specified, the model was solved for 50k steps on a working station laptop (processor: i7-11800H @ 2.30 GHz / RAM: 32 GB) using Matlab 2023b with a step size of $\tau = 0.1$ ms. The parameters γ_1 , γ_2 , and γ_3 in (47) were set to 1, -0.015 , 0.1, respectively. The threshold ϵ in (48) was set to $\epsilon = 1 \times 10^{-6}$ and the maximum iteration was 150 (not reached in any simulation). Each measurement recorded

TABLE I
 MACHINE PARAMETERS

Parameter (stator)	Value	Parameter (stator)	Value
Inner radius [mm]	32.077	Outer radius [mm]	60
Stack length [mm]	80	Number of slots	24
Tooth base length [mm]	11.945	Tooth base width [mm]	4.75
Tooth head length [mm]	0.6	Tooth head width [mm]	6.078
Number of turns per slot	66	Phase belt [deg]	60
Phase winding resistance [Ω]	6.2	Phase leakage inductance [mH]	6.235
Parameter (rotor)	Value	Parameter (rotor)	Value
Inner radius [mm]	5.975	Outer radius [mm]	31.6
Stack length [mm]	80	Number of slots	17
Tooth base length [mm]	11.2	Tooth base width [mm]	5.25
Tooth head length [mm]	0.4	Tooth head width [mm]	10.216
Inertia [$\text{kg}\cdot\text{m}^2$]	0.0011	Damping [$\text{N}\cdot\text{m}\cdot\text{s}/\text{rad}$]	0.0005
Bar resistance [$\mu\Omega$]	78.09	Ring segment resistance [$\mu\Omega$]	2.5988
Bar leakage permeance [nH]	67.6	Ring segment leakage permeance [nH]	0.9273

one million datum points for all channels under a sampling frequency of 250 kHz. Both simulations and measurements implemented a rated power supply and a "star" winding connection with an isolated neutral point.

A. Determination of the Number of Slices

To select an appropriate number of slices, the magnetic co-energy stored in the air gap and the input electrical power were simulated under a locked rotor condition with different slice numbers. The simulation results are presented in Fig. 7. Overall, as the slice number increases, both the magnetic co-energy and input electrical power converge. Additionally, the time consumption increases quadratically, even though the number of unknowns grows linearly.

Based on the above observations, the number of slices is chosen to be the minimum such that the discretisation errors (relative to the values obtained using ten slices) fall below a certain threshold. Here, a threshold of 0.5% was considered, leading to a slice number of $N = 5$. Specifically, the errors for $N = 5$ are 0.3484% for the magnetic co-energy and 0.0016% for the input electrical power. Additionally, at other rotor speeds, the errors are found to be generally smaller than those presented in Fig. 7. Therefore, we conclude that using five slices is sufficient for modelling this machine. In the remainder of this section, the simulation results were obtained using five slices.

Furthermore, Fig. 7 illustrates that a multi-slice MEC achieves a computational cost balance between a 2D MEC model and a 3D MEC model. Specifically, the multi-slice model (with $3+N_r+3N(N_s+N_r)$ unknowns) reduces to a 2D model (with $3+N_r+3(N_s+N_r)$ unknowns) if $N = 1$, and it extends to a 3D model (with $3+N_r+(5N-2)(N_s+N_r)$ unknowns) if axial fluxes are considered. Back to our earlier choice of five slices, the proposed multi-slice method has 635 unknowns that need to be solved simultaneously at every time step and requires 10.77 times more computation time (1708.35 s) compared to a 2D model (143 unknowns, 158.64 s), while an extended 3D model has 963 unknowns and is estimated to require 24.24 times more time (3844.71 s).

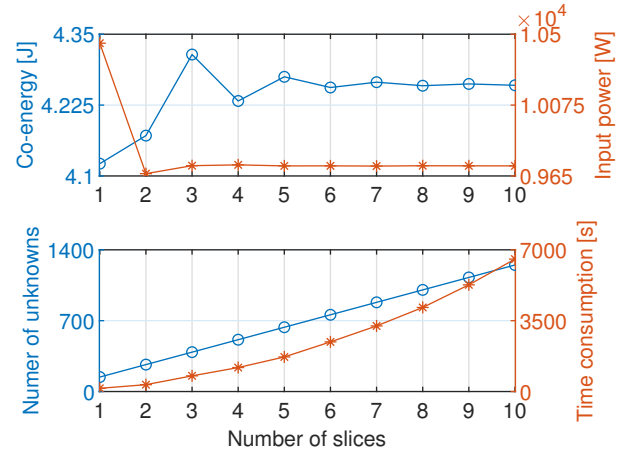


Fig. 7. Results of locked rotor simulations with the slice number ranging from 1 (axial nonuniformity neglected) to 10.

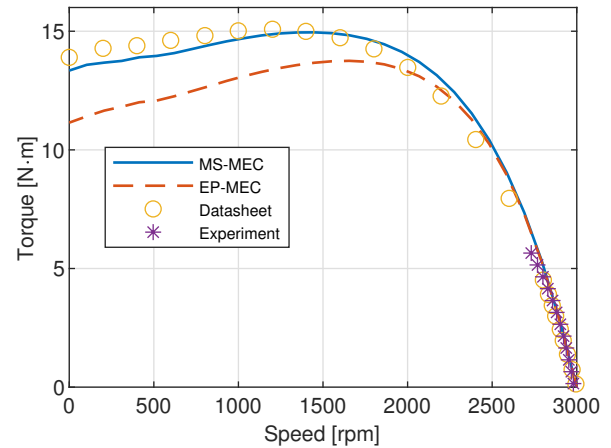


Fig. 8. Steady-state torques of the machine obtained from the MS-MEC model, the EP-MEC model, the datasheet, and the experiment.

B. Model Validation: Skewed Machine

The machine static performance was simulated using the proposed multi-slice MEC-based model with a time-step of 1 ms. The data obtained from both the experiment and the machine datasheet are used as the reference. Additionally, the results obtained using the recently developed equivalent air gap permeance calculation-based MEC model [26] were added for comparison. In the remainder of this section, for simplicity, we refer to these two MEC-based models as MS-MEC model and EP-MEC model, respectively.

Figure 8 compares the simulated and measured steady-state torque-speed characteristics of the machine operating at the nominal voltage and frequency. Both the proposed MS-MEC model and the EP-MEC model predict accurate torques at the machine working points, i.e., at the low slips. However, the produced torque at a high slip predicted by the EP-MEC model is deviated from the reference. This implies an underestimated air gap flux density, which may stem from the equivalent air gap permeance calculation. The discrepancy between the proposed method and the measurements can be attributed in part to the estimation of the rotor bar resistance, as it is

TABLE II
MACHINE PERFORMANCE AT DIFFERENT LOAD CONDITIONS

Data Source	Load [%]	I [A]	P1 [kW]	P2 [kW]	Speed [rpm]	cos φ	η [%]
MS-MEC	125	2.87	1.66	1.36	2815	0.841	81.84
EP-MEC	125	2.84	1.66	1.36	2814	0.847	81.92
Datasheet	125	2.96	1.70	1.38	2818	0.829	80.94
MS-MEC	100	2.46	1.33	1.10	2856	0.782	82.99
EP-MEC	100	2.43	1.33	1.10	2854	0.790	83.09
Datasheet	100	2.51	1.34	1.10	2861	0.770	82.07
MS-MEC	75	2.13	1.01	0.84	2893	0.687	83.10
EP-MEC	75	2.09	1.01	0.84	2892	0.698	83.26
Datasheet	75	2.15	1.00	0.83	2900	0.677	81.92
MS-MEC	50	1.89	0.70	0.57	2929	0.536	81.02
EP-MEC	50	1.84	0.70	0.57	2928	0.549	81.27
Datasheet	50	1.88	0.70	0.55	2934	0.534	79.14
MS-MEC	25	1.77	0.40	0.29	2962	0.328	72.25
EP-MEC	25	1.70	0.40	0.29	2962	0.338	72.54
Datasheet	25	1.73	0.40	0.28	2966	0.335	68.41

Remark: I, P1, P2, cos φ , and η denote the stator current RMS, input active power, output mechanical power, power factor, and efficiency.

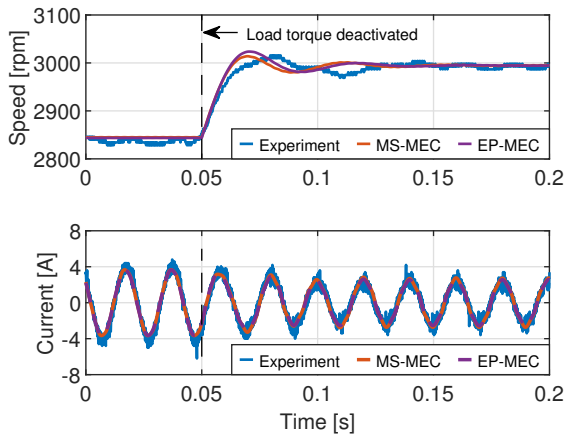


Fig. 9. Comparison on the transient stator phase winding current and rotor speed under a sudden change in the load torque.

affected by the skin effect that is not considered in this work.

An accurate prediction of IM performance at low slips is crucial since the majority of IMs are operated at speeds that are close to the synchronous speed. Table II details the performance metrics of the machine under different loads. The average percentage errors of the MS-MEC model, across all load conditions, for stator current, rotor speed, power factor, and efficiency are 1.76%, 0.17%, 1.39%, and 2.33%, respectively. These errors of the EP-MEC model are 2.78%, 0.20%, 2.32%, and 2.56%, respectively. Overall, the multi-slice approach provides a slightly better approximation of the machine behavior at typical working points.

Figure 9 compares the transients of the stator phase winding currents and rotor speed caused by a sudden change in the load torque (from 4 N·m to 0 N·m). Here, the experimental data were sampled at 5 GHz to precisely capture the encoder pulses. All three sources indicate that the stator current reaches the new steady-state within approximately three electrical periods. However, noticeable discrepancy in the rotor speed is observed. Both simulation models show a larger acceleration at the beginning of the transient and underestimate the time needed to reach the new steady-state speed. The MS-MEC

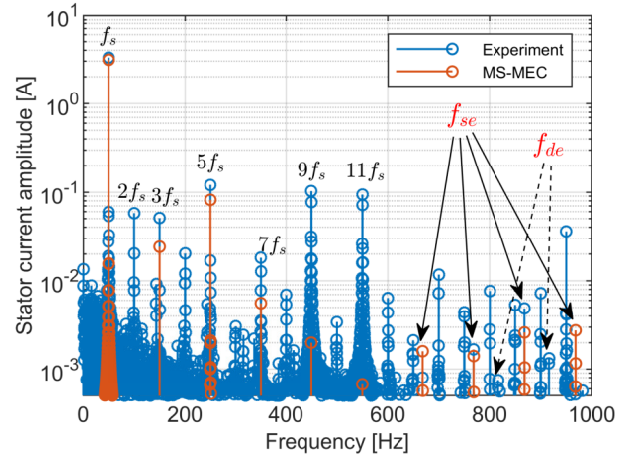


Fig. 10. Stator current comparison in the frequency domain. The test machine experiences a 25% static eccentricity at the non-load end.

model predicts a peak speed closer to the measured speed than the EP-MEC. The discrepancy between the simulations and the experiment in the speed transient may stem from the simplified mechanical model and idealised load torque jump used in the simulations.

C. Model Validation: Skewed Machine with Axially Nonuniform Eccentricity

Since the equivalent air gap permeance approach has not been extended to cover both skew and arbitrary rotor inclination, this section focuses the comparison between the proposed model and the experimental results for different eccentric scenarios. The comparisons were made in the frequency domain as the eccentricity-triggered characteristics are inconspicuous in the time domain. For both the simulations and experiments, the frequency spectra were obtained by performing the fast Fourier transform on the data recorded in a four-second-long window.

Figure 10 shows the comparison results of the stator currents recorded at the steady state, where the machine operates at 2882 rpm with a static eccentricity of 25% introduced at the non-load end by adjusting the external bearing housing mounting positions in Fig. 6. The fundamental frequency component, observed at the supply frequency f_s , is dominant in the spectrum, followed by its integer-order harmonics. The odd order harmonics mainly due to the saturation are predicted by the MEC, while the even order harmonics are not since they stem from the unbalance that are not considered in the simulation. The spectral characteristics observed in the measured current spectrum are much broader and encompass minor peaks that are not predicted by the MEC model. Such disparities are anticipated as slight asymmetries inherent in the physical system and the pulse-width modulation supply voltage can broaden spectral features and introduce additional frequency components. Additionally, the predicted harmonics are generally smaller in amplitude than those measured, since the factors mentioned above as well as the errors in approximating the material B-H curve and other machine parameters contribute to the inaccuracy in current distortion prediction.

TABLE III
PSH AMPLITUDE COMPARISON

Frequency component	Eccentricity	Amplitude [mA]				
		0% load	25% load	50% load	75% load	100% load
Lower PSH (Simulation)	0% ecc.	0.00	0.00	0.01	0.01	0.01
	25% ecc.	1.68	1.43	1.20	1.06	1.37
	Increment	1.68	1.43	1.19	1.05	1.36
Lower PSH (Experiment)	0% ecc.	2.14	1.82	1.61	1.44	1.53
	25% ecc.	2.07	2.16	1.53	1.67	1.80
	Increment	-0.07	0.34	-0.08	0.23	0.17
Upper PSH (Simulation)	0% ecc.	0.00	0.00	0.00	0.01	0.01
	25% ecc.	1.48	1.88	2.09	2.03	2.29
	Increment	1.48	1.88	2.09	2.02	2.28
Upper PSH (Experiment)	0% ecc.	3.74	3.14	3.05	2.83	3.40
	25% ecc.	4.10	5.14	3.23	4.87	5.34
	Increment	0.36	2.00	0.18	2.04	1.94

Specifically, The relative errors of 1st-, 3rd-, and 5th-order harmonic amplitudes are 5.6%, 51.8%, and 32.3%, respectively. The simulated static eccentricity-induced fault characteristic frequencies f_{se} are observed at 668.48 Hz, 768.48 Hz, 868.48 Hz, and 968.48 Hz, respectively. These frequencies align well with those measured with errors below 1%. These frequency components are present at the rotor slot harmonic frequencies, and the 768.48 Hz and 868.48 Hz component are the lower and upper principle slot harmonics (PSHs) [6]. The errors in lower and upper PSH amplitudes are 15.7% and 46.4%, respectively. Moreover, the dynamic eccentricity-induced frequencies f_{de} are found only in the measured currents at 816.50 Hz and 916.50 Hz. This clearly illustrates that the test machine has an inherent dynamic eccentricity, which may be attributed to the modified shaft supporting structure, the manufacturing imprecision, and the wear of the bearing.

Table III compares the PSH amplitudes across various load and inclined eccentricity conditions. Overall, the simulated PSH amplitudes tend to increase as the eccentricity level rises, with the upper PSH being notably larger than the lower PSH. Most experimental results confirm these trends. Due to the inherent eccentricity, the measured PSH amplitudes at non-eccentric conditions are much higher than those predicted. Moreover, both simulations and experiments show that the PSH amplitudes do not monotonically increase with heavier loads. This is because equalising currents induced in the rotor cage of an IM tend to dampen the asymmetry in fields due to eccentricity [32]. Specifically, the average errors of lower PSH and upper PSH amplitudes across all load conditions at 25% inclined eccentricity are 26.9% and 55.6%, respectively. The simulated upper PSH amplitude increments at relatively high loads are close to those measured. The relative errors are 1% and 17.5% at 75% load and 100% load, respectively. Despite the accurate prediction of the fault characteristic frequencies, the simulated and measured amplitudes of eccentricity-induced frequency components are less aligned. This discrepancy may be attributed to the susceptibility of small harmonic amplitudes to factors such as measurement noise.

VI. CONCLUSION

A multi-slice MEC-based modelling has been presented to model axial nonuniformity in an IM. The proposed method

neglects axial fluxes and divides a machine into 2D slices. Each slice remains axially uniform with its length, angular displacement, and radial translation determined by Gaussian discretisation. All slices share an identical current excitation. The good alignment between the simulated and measured data shows that the proposed model is capable of predicting the behaviour of an IM with axial nonuniformity. The computational cost of the multi-slice MEC is considerably less than that of a 3D MEC for an equal number of axial nodes. Additionally, this study finds that the amplitudes of eccentricity-induced frequency components in stator currents generally show an increase with the escalating fault severity, and load can lead to alleviated current harmonics. Notably, the fault-induced harmonics exhibit small amplitudes, rendering them susceptible to factors such as measurement noise. This implies that using harmonic amplitudes as a fault severity indicator can be challenging in practical applications.

REFERENCES

- [1] L. Wang, X. Bao, C. Di, and J. Li, "Effects of novel skewed rotor in squirrel-cage induction motor on electromagnetic force," *IEEE Trans. Magn.*, vol. 51, no. 11, pp. 1–4, 2015.
- [2] W. Xu, X. Bao, C. Di, L. Wang, and Y. Chen, "Optimal angle combination for improving electromagnetic torque in induction motor with double-skewed rotor," *IEEE Trans. Magn.*, vol. 53, no. 11, pp. 1–5, 2017.
- [3] X. Li, Q. Wu, and S. Nandi, "Performance analysis of a three-phase induction machine with inclined static eccentricity," *IEEE Trans. Ind. Appl.*, vol. 43, no. 2, pp. 531–541, 2007.
- [4] M. Ojaghi and M. Mohammadi, "Unified modeling technique for axially uniform and nonuniform eccentricity faults in three-phase squirrel cage induction motors," *IEEE Trans. Ind. Electron.*, vol. 65, no. 7, pp. 5292–5301, 2018.
- [5] D. G. Dorrell, J. K. H. Shek, M. A. Mueller, and M.-F. Hsieh, "Damper windings in induction machines for reduction of unbalanced magnetic pull and bearing wear," *IEEE Trans. Ind. Appl.*, vol. 49, no. 5, pp. 2206–2216, 2013.
- [6] Z. Gong, P. Desenfans, D. Pissort, H. Hallez, and D. Vanoost, "Multi-physics coupling model to characterise the behaviour of induction motors with eccentricity and bearing faults," *IEEE Trans. Energy Convers.*, vol. 39, no. 1, pp. 146–159, 2024.
- [7] V. Ostovici, *Dynamics of Saturated Electric Machines*. New York, NY, USA: Springer-Verlag, 1989.
- [8] H. De Gersem and L. A. M. D'Angelo, "Modeling skew by single- and multi-slice 2-d machine models," *IEEE Trans. Magn.*, vol. 57, no. 6, pp. 1–4, 2021.
- [9] D. Zhang, T. Liu, C. He, and T. Wu, "A new 2-d multi-slice time-stepping finite element method and its application in analyzing the transient characteristics of induction motors under symmetrical sag conditions," *IEEE Access*, vol. 6, pp. 47 036–47 046, 2018.
- [10] R. S. C. Pal and A. R. Mohanty, "A simplified dynamical model of mixed eccentricity fault in a three-phase induction motor," *IEEE Trans. Ind. Electron.*, vol. 68, no. 5, pp. 4341–4350, 2021.
- [11] S. D. Sudhoff, B. T. Kuhn, K. A. Corzine, and B. T. Branecky, "Magnetic equivalent circuit modeling of induction motors," *IEEE Trans. Energy Convers.*, vol. 22, no. 2, pp. 259–270, 2007.
- [12] R. Wang, S. Pekarek, P. O'Regan, A. Larson, and R. van Maaren, "Incorporating skew in a magnetic equivalent circuit model of synchronous machines," *IEEE Trans. Energy Convers.*, vol. 30, no. 2, pp. 816–818, 2015.
- [13] H. Saneie and Z. Nasiri-Gheidari, "Performance analysis of outer-rotor single-phase induction motor based on magnetic equivalent circuit," *IEEE Trans. Ind. Electron.*, vol. 68, no. 2, pp. 1046–1054, 2021.
- [14] G. Forstner, A. Kugi, and W. Kemmetmüller, "A magnetic equivalent circuit based modeling framework for electric motors applied to a pmsm with winding short circuit," *IEEE Trans. Power Electron.*, vol. 35, no. 11, pp. 12 285–12 295, 2020.
- [15] R. Alipour-Sarabi, Z. Nasiri-Gheidari, and H. Oraee, "Development of a three-dimensional magnetic equivalent circuit model for axial flux machines," *IEEE Trans. Ind. Electron.*, vol. 67, no. 7, pp. 5758–5767, 2020.

- [16] G. Watthewaduge and B. Bilgin, "Reluctance mesh-based magnetic equivalent circuit modeling of switched reluctance motors for static and dynamic analysis," *IEEE Trans. Transp. Electrification*, vol. 8, no. 2, pp. 2164–2176, 2022.
- [17] P. Naderi and A. Shiri, "Rotor/stator inter-turn short circuit fault detection for saturable wound-rotor induction machine by modified magnetic equivalent circuit approach," *IEEE Trans. Magn.*, vol. 53, no. 7, pp. 1–13, 2017.
- [18] A. Hemeida, M. M. Billah, K. Kudelina, B. Asad, M. U. Naseer, B. Guo, F. Martin, P. Rasilo, and A. Belahcen, "Magnetic equivalent circuit and lagrange interpolation function modeling of induction machines under broken bar faults," *IEEE Trans. Magn.*, vol. 60, no. 3, pp. 1–4, 2024.
- [19] W. Tong, S. Li, X. Pan, S. Wu, and R. Tang, "Analytical model for cogging torque calculation in surface-mounted permanent magnet motors with rotor eccentricity and magnet defects," *IEEE Trans. Energy Convers.*, vol. 35, no. 4, pp. 2191–2200, 2020.
- [20] Q. Han, Z. Ding, X. Xu, T. Wang, and F. Chu, "Stator current model for detecting rolling bearing faults in induction motors using magnetic equivalent circuits," *Mech. Syst. Signal Process.*, vol. 131, pp. 554–575, 2019.
- [21] Q. Han, T. Wang, Z. Ding, X. Xu, and F. Chu, "Magnetic equivalent modeling of stator currents for localized fault detection of planetary gearboxes coupled to electric motors," *IEEE Trans. Ind. Electron.*, vol. 68, no. 3, pp. 2575–2586, 2021.
- [22] P. Desenfans, Z. Gong, D. Vanoost, K. Gryllias, J. Boydens, and D. Pisssoort, "The influence of the unbalanced magnetic pull on fault-induced rotor eccentricity in induction motors," *J. Vib. Control*, vol. 30, no. 5–6, pp. 943–959, 2024.
- [23] N. R. Tavana and V. Dinavahi, "Real-time nonlinear magnetic equivalent circuit model of induction machine on fpga for hardware-in-the-loop simulation," *IEEE Trans. Energy Convers.*, vol. 31, no. 2, pp. 520–530, 2016.
- [24] X. Sun, K. Diao, G. Lei, Y. Guo, and J. Zhu, "Real-time hil emulation for a segmented-rotor switched reluctance motor using a new magnetic equivalent circuit," *IEEE Trans. Power Electron.*, vol. 35, no. 4, pp. 3841–3849, 2020.
- [25] J. Lannoo, D. Vanoost, J. Peuteman, S. Debruyne, H. De Gersem, and D. Pisssoort, "Improved air gap permeance model to characterise the transient behaviour of electrical machines using magnetic equivalent circuit method," *Int. J. Numer. Modell. Electron. Networks Devices Fields.*, vol. 33, no. 5, p. e2749, 2020.
- [26] P. Desenfans, Z. Gong, D. Vanoost, K. Gryllias, J. Boydens, H. De Gersem, and D. Pisssoort, "Improved air gap permeance modelling for single-slice magnetic equivalent circuits of skewed induction motors," *Compel-Int. J. Comp. Math. Electr. Electron. Eng.*, vol. 43, no. 3, pp. 475–492, 2024.
- [27] M. Amrhein and P. T. Krein, "3-d magnetic equivalent circuit framework for modeling electromechanical devices," *IEEE Trans. Energy Convers.*, vol. 24, no. 2, pp. 397–405, 2009.
- [28] M. Amrhein and P. T. Krein, "Induction machine modeling approach based on 3-d magnetic equivalent circuit framework," *IEEE Trans. Energy Convers.*, vol. 25, no. 2, pp. 339–347, 2010.
- [29] J. Faiz and M. Ghasemi-Bijan, "Estimation of induction machine inductances using three-dimensional magnetic equivalent circuit," *IET Electr. Power Appl.*, vol. 9, no. 2, pp. 117–127, 2015.
- [30] J. Gyselincx, L. Vandeveldel, and J. Melkebeek, "Multi-slice fe modeling of electrical machines with skewed slots-the skew discretisation error," *IEEE Trans. Magn.*, vol. 37, no. 5, pp. 3233–3237, 2001.
- [31] W. H. Press, *Numerical recipes 3rd edition: The art of scientific computing*. Cambridge university press, 2007.
- [32] A. Tenhunen, T. Holopainen, and A. Arkkio, "Effects of equalizing currents on electromagnetic forces of whirling cage rotor," in *Proc. IEEE Int. Electr. Mach. Drives Conf.*, vol. 1, pp. 257–263 vol.1, 2003.



Zifeng Gong (Graduate Student Member, IEEE) was born in 1996. He received his Bachelor's and Master's degrees in Electrical Engineering from Southwest Minzu University, China and from Southwest Jiaotong University, China in 2018 and 2021, respectively. He is currently a Ph.D. researcher with the Mechatronics Group (M-Group), KU Leuven, Belgium. His research interests mainly include system modelling and condition monitoring for electric machines.



Philip Desenfans was born in 1998. He received the M.S. degree in energy engineering technology from KU Leuven, Bruges, Belgium in 2021. He is currently working toward the Ph.D. degree in KU Leuven with the Mechatronics Group (M-Group) from September 2021. His current research topics are condition monitoring and active fault mitigation in electrical drives using data-driven machine-learning methods.



Davy Pisssoort (Senior Member, IEEE) was born in 1978. He received the M.S. and Ph.D. degrees in electrical engineering from Ghent University, Ghent, Belgium, in 2001 and 2005, respectively. From October 2005 to October 2006, he was a Postdoctoral Researcher at Ghent University. From November 2006 to July 2009, he was a Research Engineer in the Eesof-EDA Department, Agilent Technologies, Belgium. Since 2009, he is a professor at KU Leuven Bruges Campus, where he is the head of the Mechatronics Group. He is also affiliated with Flanders Make, as part of the Flanders Make@KU Leuven Core Lab MPro. His current research interests include the development of fast and efficient electromagnetic modelling methods for EMC, SI, and PI, the development of characterisation methods for shielding materials and gaskets, EM Resilience, dependability of autonomous systems as well as the analysis and testing of the mechanical and thermal reliability of electronic modules. Dr. Pisssoort is a Senior Member of the IEEE EMC Society, IEEE EMC Society Board Member and member of the International Steering Committee of EMC Europe.



Hans Hallez (Member, IEEE) received the master's degree in computer science from Ghent University, Ghent, Belgium, in 2003, and the Ph.D. degree in engineering science from the Faculty of Engineering and Architecture, Ghent University in 2008. He was a Postdoctoral Fellow with Ghent University from 2008 to 2011. He has been active with Bruges Campus at KU Leuven, Bruges, Belgium, as a Lecturer since 2011 and he became a Staff Member of the Faculty of Engineering Technology, KU Leuven Department of Computer Science in 2014. He became an Associate Professor with the Bruges Campus of KU Leuven in 2020. He is also a Principal Instructor of several bachelor's and master's courses at the Faculty of Engineering Technology. He is a member of the M-Group Research Group and the imec.Distrinet Research Group and focusses on edge computing of machine learning within the application of sensors and sensor networks for industrial manufacturing machines and healthcare.



Dries Vanoost (Member, IEEE) obtained his M.S. degree in electrical engineering from KU Leuven Technology Campus Ostend, Ostend, Belgium, in 2010. He then pursued a PhD degree in electrical engineering from KU Leuven, Leuven, Belgium, which he completed in 2015. Following that, he worked as a Postdoctoral Researcher at the M-Group research group, KU Leuven Bruges Campus, specializing in the global dependability of mechatronic systems and electromagnetic compatibility, from January 2016 to September 2019. In 2019, he was appointed as the M-Group research manager at the KU Leuven Bruges Campus, where he currently acts as the primary contact and interface for technology transfer, bridging the gap between industry and academia. He is also a member of the University Core Lab Flanders Make @ KU Leuven Motion Products. His research interests encompass the development of dependable interconnected mechatronic systems, electromagnetic modelling, power electronics, and power quality. He is an member of the IEEE and is affiliated with the IEEE EMC Society Benelux chapter.